Volume 1 | Number 1 | Jan 2013 | Pages 1–100

ChemComm

Chemical Communications
www.rsc.org/chemcomm

ROYAL SOCIETY OF CHEMISTRY

This is an *Accepted Manuscript*, which has been through the Royal Society of Chemistry peer review process and has been accepted for publication.

Accepted Manuscripts are published online shortly after acceptance, before technical editing, formatting and proof reading. Using this free service, authors can make their results available to the community, in citable form, before we publish the edited article. We will replace this *Accepted Manuscript* with the edited and formatted *Advance Article* as soon as it is available.

You can find more information about *Accepted Manuscripts* in the **Information for Authors**.

Please note that technical editing may introduce minor changes to the text and/or graphics, which may alter content. The journal's standard **Terms & Conditions** and the **Ethical guidelines** still apply. In no event shall the Royal Society of Chemistry be held responsible for any errors or omissions in this *Accepted Manuscript* or any consequences arising from the use of any information it contains.

ROYAL SOCIETY OF CHEMISTRY

www.rsc.org/chemcomm

Journal Name

ARTICLE

Factors influencing quantitative liquid (scanning) transmission electron microscopy

P. Abellan,[a] T. J. Woehl,[b,*] L.R. Parent,[a] N.D. Browning,[a] J.E. Evans,[c] and I. Arslan[d] ,

One of the experimental challenges in the study of nanomaterials in liquids in the (scanning) transmission electron microscope ((S)TEM) is gaining quantitative information. A successful experiment in the fluid stage will depend upon the ability to plan for sensitive factors such as the electron dose applied, imaging mode, acceleration voltage, beam-induced solution chemistry changes, and the specifics of solution reactivity. In this paper, we make use of a visual approach to show the extent of damage of different instrumental and experimental factors in liquid samples imaged in the (S)TEM. Previous results as well as new insights are presented to create an overview of beam-sample interactions identified for changing imaging and experimental conditions. This work establishes procedures to understand the effect of the electron beam on a solution, provides information to allow for a deliberate choice of the optimal experimental conditions to enable quantification, and identifies the experimental factors that require further analysis for achieving fully quantitative results in the liquid (S)TEM.

Introduction

With the development of fluid stages and the advances in microfabrication, imaging liquids in the electron microscope is now becoming a routine technique. *In situ* liquid transmission electron microscopy (TEM) and scanning TEM (STEM) using environmental fluid stages, has already been applied to the study of the electrochemical deposition of copper[1] and lead,[2] growth of different nanostructures,[3-8] observation of macromolecular complexes,[9, 10] soft materials,[11-13] biological cells,[14, 15] the lithiation/delithiation of Si nanowire electrodes during battery cycling[16] to name a few, although the range of applications continues to increase. In the fluid stage, sealed windowed-cells are used, where a liquid layer is trapped between two thin amorphous silicon nitride membranes supported by rigid silicon chips. An opening etched in the center of each chip defines an electron transparent region where the liquid is imaged through.[17] As the field has expanded and the technique become more refined, the new challenge is obtaining reproducible data free of artifacts and beam-induced effects to enable quantitative analysis.

Phenomena such as protein conformational dynamics necessitate quantitative analysis of protein movements and structural rearrangements in liquid, while understanding nanoparticle growth dynamics and multi-particle interactions requires measurement of particles size and inter-particles distances over time. Since the reliability of *in situ* studies within fluid stages can be strongly affected by the electron beam, strategies to understand, minimize and eliminate beam induced artifacts continue to be needed.[18] Evaluation of the degree of radiation damage resulting from beam-induced

reactions within the liquid sample is critical for the quantitative interpretation of phenomena at the nanoscale. There have already been studies that first calibrate the effect of electron dose on a system in order to explain *in situ* data.[3, 4, 7, 19-24] Important parameters such as the threshold electron dose to induce nucleation and growth of nanoparticles by electron beam induced reduction have been determined for the growth of silver nanoparticles in solution in the STEM[4] and, by systematically tracking movement of gold nanoparticles, White and co-workers showed that increased beam currents caused charging that led to repulsion of the nanoparticles from the field of view.[23] These examples demonstrate that important physical and chemical phenomena can be systematically exploited to calibrate the effect of electron dose on *in situ* liquid imaging experiments. Besides electron dose, factors such as accelerating voltage, imaging mode (e.g. TEM, STEM, SEM), liquid thickness, and solution composition are expected to affect the results of *in situ* experiments.

By using spherical aberration corrected microscopes under low dose conditions, atomic scale imaging and chemical analysis can be achieved, with improved resolution for thinner membrane thicknesses and fluid path lengths.[3, 25] Experimental spatial resolution values reported by different research groups using Au and PbS nanoparticles are found to be in good agreement with theoretical maximal spatial resolution values dependent on liquid thickness for TEM and STEM imaging modes.[17] This means that the ultimate limitation to the spatial resolution in the fluid stage is the local structural damage caused by the electron beam on the sample (liquid or/and solid matter therein). Therefore, the sample-beam interaction, not only determines the reproducibility and accuracy of *in situ* fluid cell STEM data, but also the attainable spatial resolution.

Here we present our analysis of the effects of different experimental and technical parameters (e.g. imaging mode, beam current) that control the amount of electron dose applied to the system and also the way it is delivered. We review previous results as well as present new insights into the effect of the electron dose applied, the accelerating voltage, and imaging mode. Other factors affecting quantification, such as precursor depletion and accumulation of residual radicals over time are discussed. Finally, we emphasize the importance of complementing the *in situ* analysis with post-mortem analysis of reaction products to ensure that the reactivity of the sample has not misled quantification.

## 1. Calibrating the effect of electron dose in liquids

1.1 Need for dose quantification.

When high-energy electrons irradiate water or an aqueous solution, radiolytic species are formed. Water decomposes upon radiolysis forming the following compounds: e^-_{aq}, $H^\bullet$, $OH^\bullet$, H_2, H_2O_2, H^+, OH^-. The chemical species generated interact with the sample in the fluid cell and may trigger undesired reactions. The amount of radiation damage resulting from these beam-induced indirect reactions strongly depends on the electron dose delivered to the sample. For instance, in the presence of a precursor solution with metal ions, reduction of the solvated species may occur, giving rise to formation of nanoparticles from solution.[26] These radiolytic species can also lead to the formation of gaseous hydrogen in the liquid as well, in some cases forming nanobubbles in the thin liquid layer.[12, 27] *In situ* growth of nanoparticles in solution induced by the electron beam is well known to occur via (S)TEM irradiation.[3, 4, 19, 20]

Recently, it was demonstrated that by controlling the electron dose delivered to the liquid sample, this "undesired" reaction can act as a surrogate for chemical reduction and be exploited to provide insight into the mechanisms of nanoparticle growth by chemical reduction.[4] Even more important for a broader number of experiments, it was determined that the STEM imaging parameters such as the electron beam current, pixel dwell time, and magnification (pixel size) can be varied to keep the dose delivered under a critical value below which no nucleation or growth induced by the electron beam is experimentally observed.[4] It is interesting to note that the critical electron dose to induce nucleation is of the same order of magnitude ($\sim$10 electrons/Å^2 for 200 kV electrons) as is typically cited as the damage threshold for cryo-TEM imaging,[24, 28] supporting the hypothesis that ionization interactions are causing the observed interactions in the liquid stage. This method for determining the threshold electron dose should be generally applicable to various reactions for various imaging modes, electron beam energies, and solution chemistries. Establishing the conditions for the damage threshold of a specific solution under the electron beam is a crucial step in obtaining reproducible quantitative information from *in situ* liquid experiments.

1.2 How to visualize dose effects.

The electron beam is both the ionizing radiation source and the probe to image our system. Damage becomes visible and can be quantified as soon as a damage variable can be identified, e.g. observations of nanoparticle nucleation. Using the methodology explained in previous work,[4] the growth of silver nanocrystals

in an *in situ* fluid stage can be used to calibrate for the effect of dose. The growth of silver nanoparticles from an aqueous silver precursor follows a simple one electron reduction reaction:[4]

$$Ag^+ + e^-_{aq} \rightarrow Ag^\circ$$
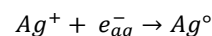
For the case of aqueous electrons, e^-_{aq}, generated during radiolysis, the amount and distribution of silver nanocrystals grown provides insights into the effect of the electron beam on liquid samples and can be quantified. This approach may provide a means to directly visualize the effects of ionizing species and estimate their relative amounts, so that a reaction can be correlated for different microscope settings and beam conditions. However, the large number of radicals and recombination reactions occurring in the liquid make quantification of all the ionization products difficult.[29]

Custom image analysis algorithms using standard thresholding methods can be used to analyze movies of the Ag nanocrystal nucleation and growth. An example of this methodology applied to a bright field (BF) STEM dataset of nucleation and growth of silver nanoparticles is shown in Fig 1(a)-(d). The total number of particles formed in each frame of the *in situ* movie, N_p, is measured as a function of time (Fig. 1(e)). Fig. 1(f) shows the time evolution of the effective radius of the six particles labeled in (a)-(d).
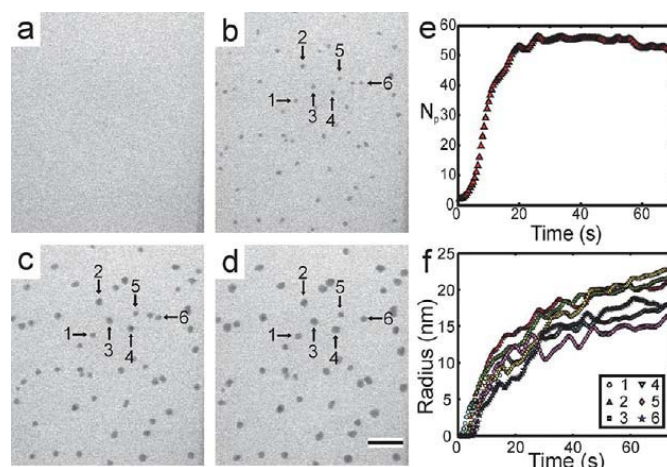

Fig 1. Time lapsed series of BF STEM images showing silver nanocrystal formation from a AgNO$_3$ precursor solution at t=0 s (a), t=15 s (b), t=45 s (c) and t=75 s (d), relative to the initial irradiation. Scale bar is 200 nm, the accelerating voltage was 200 kV and the beam current was i_e = 40 pA. The total number of particles (e) and radius of particles 1-6 (f) as a function of time. Reprinted with permission.[4] Copyright 2012 American Chemical Society.

Based on the analysis of each frame of the *in situ* movie, a threshold electron dose below which no nucleation or growth of nanocrystals occur in the field of view was determined. For the case of nanoparticle formation, the induction threshold for beam-induced nucleation provides conditions at which the amount of electron beam damage in the solution is not high enough to meet the supersaturation condition necessary for formation of stable nuclei. Knowing this variable is the first step for planning a controlled growth experiment that can be

quantified. By doing so, the same study showed that two different growth regimes exist at electron dose rates relative to the threshold electron dose rate.[4] For dose rates near the threshold value (~1.2*threshold), growth of particles was governed by a reaction limited growth mode resulting in primarily faceted nanoparticle morphologies. For higher dose rates (~7*threshold), spherical nanocrystals grow by a hindered diffusion limited mechanism, where their size increased at a rate approximately three times smaller than that predicted for the purely diffusion limited case.

2. How dose is delivered

2.1 Effect of beam energy.

Even if the electron dose conditions necessary for reproducing and controlling a reaction are found, their relation to another TEM, operating with a different acceleration voltage, is not straightforward. Changing the beam current or magnification simply changes the flux of electrons irradiating the sample; however, changing the accelerating voltage of the electrons alters the fundamental physics of the electron-fluid interaction, i.e. the cross-sections for inelastic and elastic scattering in the fluid. For example, increasing the electron energy could reduce radiolysis damage since the cross-section for inelastic scattering and associated ionization effects would be smaller.[30, 31] Furthermore, beam broadening would be lowered and thus resolution enhanced, since the cross-section for elastic scattering will be reduced. However, other types of damage such as knock-on damage could be increased at higher accelerating voltages while the use of smaller acceleration voltages could make radiolysis damage more acute.[31]
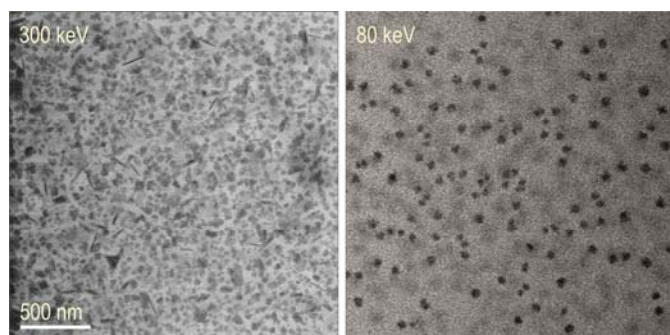

Fig 2. BF STEM images of silver nanocrystals grown from solution at 300 kV (left) and 80 kV (right). The magnification was M=40000X, pixel-dwell time was 3 μs, calibrated beam current 7.1 pA and image size was 1024x1024 pixels, which corresponded to an electron dose per frame of 39.1 e$^-$/nm^{2}f.

Fig. 2 illustrates the effect of electron energy on the growth of particles in solution for 80 keV (right) and 300 keV electrons (left). The same dose rate was used for both datasets; however, the final nanocrystal morphology is distinctly different for each accelerating voltage. The 300 kV electron beam induced the growth of a mixture of near-spherical nanoparticles, faceted triangles, needles, and cube shaped nanocrystals, with nearly 100% coverage of the viewing area (Fig. 2 left). The 80 kV electron beam caused formation of a relatively smaller amount of nanocrystals all with near-spherical morphology (Fig. 2

right). During prior experiments, the effect of electron beam current on the growth kinetics and on the final morphology of Ag nanocrystals has been observed using a 200 kV accelerating voltage.[4] Near-spherical shapes, similar to those grown by 80 kV electrons were found when delivering relatively high electron doses, for which growth qualitatively followed a diffusion limited process. A mixture of near-spherical and faceted nanocrystals, like those found when using 300 kV electrons, were found for lower doses, suggesting that for the same dose rate, the effect of 300 kV electrons is qualitatively similar to applying a lower electron dose for the same energy. However, the overall area of silver growth is larger at 300 kV, which does not exactly match the trend of a lower effective dose rate as compared to 80 kV acceleration voltage. These results show that the damaging effect of electrons in liquid samples cannot be simply explained just by considering the electron flux and concentration of reducing radicals created. As mentioned earlier, oxidizing radicals are also created during radiolysis of the liquid; one explanation may be that the relative amount of these radicals was increased at 80 kV, leading to a significant back reaction that may inhibit nanocrystal growth. A more detailed quantitative study of the effect of accelerating voltage on nanoparticle growth is warranted to elucidate the differences in the electron beam-sample interactions between 80 and 300 kV.

2.2 Global versus local irradiation.

Another challenge when reproducing experiments in different electron microscopes is the imaging mode. The choice of imaging mode in transmission electron microscopy is typically made by considering the different capabilities they offer. While TEM provides higher time resolution when compared to STEM (although a method for higher speed STEM acquisition for liquids has been recently proposed[21]) and typically higher spatial resolution, STEM offers enhanced contrast for many materials, and allows for imaging of thick liquid samples on the order of microns.[32] However, a direct comparison of the electron-liquid interactions for the TEM and STEM imaging modes has not been provided.

First, we must consider the intrinsic differences in the way electrons are delivered to the sample to form an image. In STEM, a focused beam (~1 Å or less in spherical aberration corrected instruments) is scanned across the sample and scattered signals are collected and serially integrated on the detector to form each pixel intensity. Therefore, a large amount of electrons are delivered to the specimen in a very small area during a time interval given by the dwell time, typically 0.5 - 5 μs duration. The minimum total time required to form an image in STEM is about 500 ms - this is the minimum time interval that must pass until the beam is incident onto the same area of the sample for the next subsequent scan.

On the other hand, when using TEM imaging, a parallel, continuous flux of electrons is delivered over an extended area of the sample (typically tens of microns beam size at low magnifications). While the amount of electrons per pixel per unit of time delivered in TEM is orders of magnitude smaller than that in STEM, the cumulative dose after the total exposure time in such static image configuration may be considerably higher. For the case of TEM, the total exposure time to collect an image is 25ms or higher. Fig. 3 shows four frames from different BF STEM (a)-(c) and TEM (d) movies of beam-induced growth of Ag. The time passed since electron irradiation started is shown in the bottom right corner.
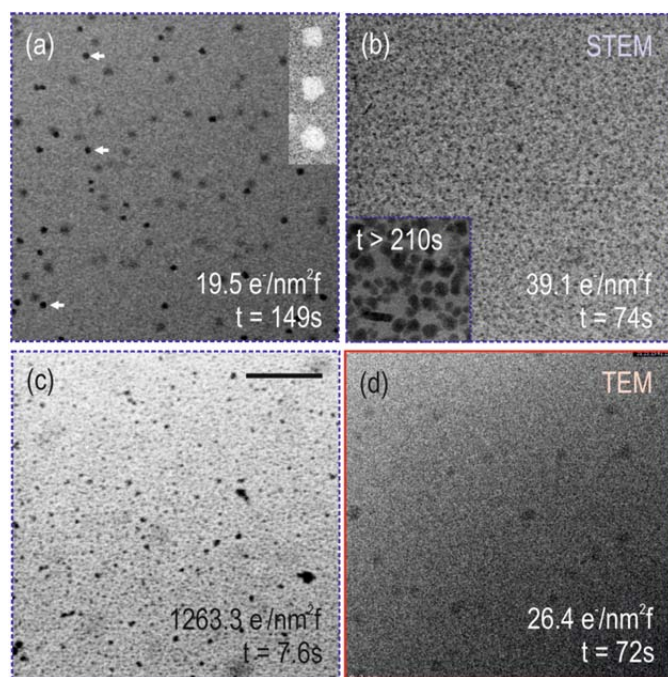
Fig 3. Nanocrystal growth under varying dose and imaging mode conditions. Image size was 1024x1024 pixels with pixel sizes of 4.1 nm^2 (a)-(c) and 4.4 nm^2 (d). Scale bar is 500 nm and is the same for all of the images. Acceleration voltage was 300 kV. In STEM mode, a 3 μs pixel-dwell time and electron beam currents of (a) 3.5 pA corresponding to an electron dose per frame of 19.5 e$^-$/nm^{2}f, (b) 7.1 pA to give 39.1 e$^-$/nm^{2}f and (c) 25.9 pA corresponding to 1263.3 e$^-$/nm^{2}f. Insets in (a) are digitally magnified images of the three particles indicated by arrows, using the corresponding high angle annular dark field (HAADF) image recorded simultaneously. Inset in (b) is a cropped image taken at higher magnification (area size is 400 nm x 400 nm) of a later stage of growth of the nanocrystals, where their morphology can be better distinguished. The cumulative dose for the three STEM images is approximately the same. (d) In TEM mode the total exposure time was 0.3 s, with an electron beam spread over a 15.3 μm region on the sample. The beam current was i$_e$=2600 pA, corresponding to a dose rate per frame of 26.4 e$^-$/nm^{2}f. The total irradiation times are indicated in the images.

In order to perform a quantitative comparison, it is also important to know how electron dose values are calculated for each imaging mode (included in the experimental section). The magnification was M = 40000x for STEM imaging (a)-(c) and M = 10000x for TEM, yielding a similar pixel size of 4.1nm^2 for STEM and 4.4 nm^2 for TEM. All the images in Figures 3 and 4 have been cropped and digitally scaled to the same magnification to account for the small differences in pixel size between the pre-set magnifications in TEM and STEM modes. The values of the calibrated electron beam currents at the sample for the different images in Fig. 3 are shown in Table I. The pixel dwell time for all STEM images was 3 μs, with a total acquisition time of ~3.78 s, which also accounts for the scan flyback time occurring outside the image area. The exposure time in TEM was 0.3 s. The beam size in STEM was ~1 Å for all the measurements, while for TEM, a beam diameter of 15.3 μm was used.

Table I. Microscope parameters for the images in Fig 3

Image/ Imaging mode	Frame time (s)	Beam current (pA)	Dose per frame (e$^-$/nm^{2}f)	Frame #	Cumulative dose (e$^-$/nm^2)
(a) STEM	3.78	3.5	19.5	39	760.5
(b) STEM	3.78	7.1	39.1	20	782.0
(c) STEM	3.78	25.9	1263.3	2	2526.6
(d) TEM	0.3	2600	26.4	-	6330

Taking into account the experimental conditions for each separate mode, the electron dose per frame and correspondingly per pixel, were calculated and are indicated in Fig. 3 and in Table I. Note that for the three STEM images, each dataset was recorded using different electron dose per frame values (see Fig 3 (a)-(c)). While (a) and (b) have approximately the same cumulative electron dose (around 770 e$^-$/nm^2), (c) is almost three times larger after just two frames. The lowest beam current, shown in Fig 3(a), promotes growth of particles approaching a reaction limited regime, yielding formation of faceted particles. As the electron dose increases ((b) and (c)), growth yields formation of near spherical and polyhedral particles. Although there are differences in the number of nuclei formed and their size for TEM irradiation, (d), the nanocrystal morphology is qualitatively equivalent to that of growth for high dose rates in the STEM (cf. (b) and (c)).

Fig. 4 shows two BF images despicting the effect of longer irradiation times for two of the conditions shown in Fig. 3. Fig. 4(a) shows extended Ag growth from the STEM dataset taken using the highest dose per frame (cf. Fig. 3(c)) and Figure 4(b) shows the results of the TEM experiment from Fig. 3(d). The total imaging time is indicated in the bottom right of each images.
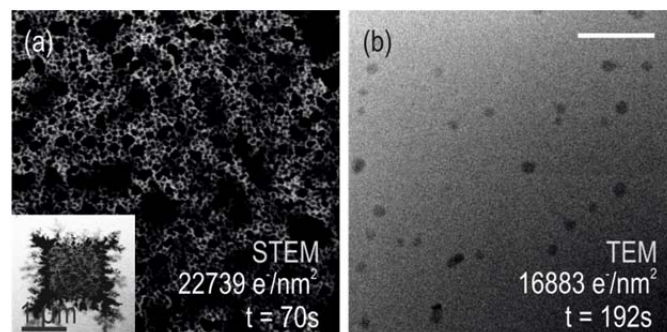

Fig 4. Silver growth evolution for (a) the highest dose STEM example in Fig 3(c) and (b) the TEM experiment in Fig 3(d). Depletion has occurred in the TEM experiment. Image size was 1024x1024 pixels with pixel sizes of 4.1 nm^2 (a) and 4.4 nm^2 (b). Scale bar is 500 nm. Acceleration voltage was 300 kV. (a) STEM BF image with 3μs pixel dwell time and electron beam current of 25.9 pA corresponding to 1263.3 e$^-$/nm^{2}f. (b) TEM image, for 0.3 s total exposure and electron beam current of 2600 pA, corresponding to a dose rate per frame of 26.4 e$^-$/nm^{2}f.

A cumulative dose of 22739 e$^-$/nm^2 has been calculated for the growth shown in Fig. 4(a), induced by a scanning probe in STEM. Besides the massive growth of Ag in the viewing area, dendritic growth of Ag is observed on the edges of the scanned region (Fig. 4(a) inset). In this case, the cumulative dose for the case of the TEM image is of the same order. Interestingly, the number of particles grown in the viewing area is much lower.

What's more, there is little change in the number of particles between Figs. 3(d) and 4(b), even though the sample has been irradiated for an additional ~120 seconds in Fig. 4(b). This suggests that the concentration of precursor in solution has been largely depleted by the time the frame in Fig. 3(d) was acquired.. In fact, in the TEM dataset, the same particles with similar particle sizes had already been formed after just 33 s of electron beam exposure, corresponding to a cumulative dose of 2901 e$^-$/nm^2. Thus, depletion of the precursor solution must have occurred and Ag growth stopped, during the first seconds of exposure.

In order to understand the differences between TEM and STEM in terms of dose delivered, several factors can be considered. In TEM, most of the electrons delivered to the system are not in the viewing area. In solid samples this fact provides flexibility with dosage and is used for lowering or increasing the dose applied to the object being imaged. In liquid samples, however, the radicals created in areas that are not in the viewing area may diffuse and interact throughout the sample, including the area being imaged. Also, when exploring growth dynamics of particles from solution, generated by electron beaminduced reduction, all the radicals created will contribute to precursor consumption (this will be discussed further in section 3). As an illustration, we can calculate the total number of electrons delivered in one frame for the STEM and TEM datasets in Fig. 4. For the case of TEM, since the beam diameter was 15.3 μm, the size of the illuminated area on the sample was A=184 μm^2. With a dose per frame of 26.4 e$^-$/nm^2, a total of $4858 \cdot 10^6$ electrons are delivered in one frame in TEM. For the case of STEM imaging, the frame size for Fig. 4 (a) was 4.28 μm^2 and the dose per frame 1263.3 e$^-$/nm^2, therefore a total of $5407 \cdot 10^6$ electrons were delivered per frame (see the experimental section for the definitions of dose per frame for each imaging mode). This means that, although the dose per frame was much smaller in TEM than in STEM, the total number of electrons delivered to the system per frame is similar. We can go even further and compare the amount of electrons delivered per unit of time (seconds). Taking into account the frame time in STEM and TEM, 3.78 s and 0.3 s respectively, the amount of electrons delivered per second are $1430 \cdot 10^6$ electrons in STEM mode and $1619.3 \cdot 10^7$ electrons in TEM. Thus, for the examples given in Fig. 4, although the dose per frame in STEM is two orders of magnitude larger than that in TEM, the total amount of electrons delivered to the sample per unit of time is one order of magnitude larger in TEM. This larger cumulative number of electrons in TEM may explain the depletion of Ag.

The differences between focused and parallel illumination could also have an influence on the number of nucleation sites per unit area and the size of particles observed in TEM as compared to STEM. The focused beam in STEM generates a large amount of electrons in a very small region, which could be sufficient to establish the supersaturation conditions needed for nucleation of silver from the precursor at many different locations much quicker than TEM. In TEM, if supersaturation conditions are not fulfilled, reactive species may diffuse away. The lower number of nuclei could have an effect on the larger final size of the crystals.

Another effect of the higher number of electrons delivered during the TEM experiment was the formation and growth of gas bubbles (Fig. 5).
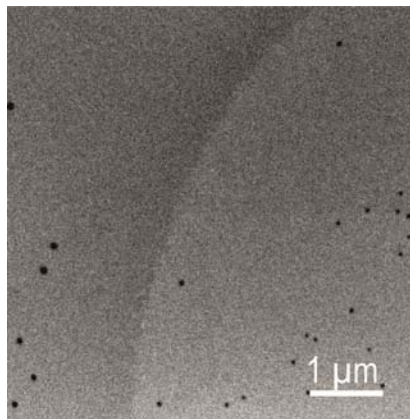

Fig 5. Low magnification BF TEM image showing the boundary between a gas bubble, displaying lighter contrast, and the liquid. Particles previously grown in solution can be seen on both sides of the bubble.

Formation of bubbles in TEM using high electron doses has been previously reported.[12, 18, 23, 33] Displacement of fluid by gas is an undesired effect in liquid experiments that has been attributed to application of high electron doses.[27, 33] Its effects on imaging quality are a sudden increase of resolution and contrast, due to the decrease of scattering events when electrons go through the gas, as compared to the fluid.

While the origin and composition of bubble formation is not clear,[18, 33] they most likely contain hydrogen gas resulting from radiolysis of the water. It is not likely that an increase in temperature causes boiling of the liquid, as previous calculations have shown the increase to be negligible in water $(0.001 - 1 \text{ K})$[20]. Biological specimens are known to produce hydrogen bubbles due to radiolysis damage[31] due to cleavage of hydrogen bonds. Interestingly, results obtained from degassed solutions show a lower frequency of bubble formation (not shown) which suggests that some of the gas in the bubble may be a result of the high-energy electrons liberating dissolved gas species.

Chemical bonds between solvent molecules may break and restore under the electron beam. This process has been observed for the case of O_2 molecules in the fluid stage under the electron beam[25]. Static irradiation in TEM, as opposed to STEM, may promote formation of bubbles formed by radiolysis because once chemical bonds of solvent molecules (mainly H bonds) are broken, their natural restoration would be limited by the continuous creation of radiolytic species in nearby regions while, in the STEM, reactive species may travel to a different area when the beam is at a different location within the scan, allowing for reformation of chemical bonds.

3. History of dose delivery

The history of the sample has a strong influence on subsequent experiments. Sample history is typically manifested as reduced nanoparticle growth due to depletion of precursor ions. Fig. 6 shows images from different image datasets recorded during the same microscope session. All of the experiments were performed in pristine areas of the sample following the order of sequence indicated with an arrow.
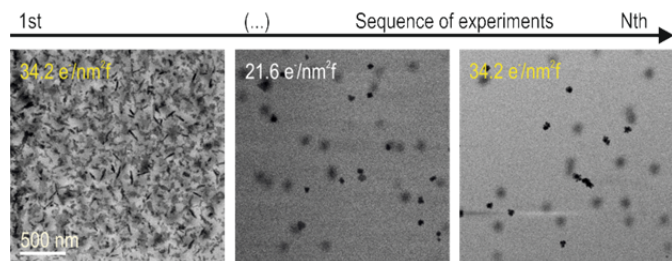
Fig. 6. Effect of precursor solution depletion and cumulative charge during a series of consecutive Ag particle growth experiments. After a number of experiments, the initial faceted and rounded nanocrystals covering the scanned area couldn't be reproduced for the same microscope conditions. BF STEM images from datasets were taken at M=40000 X magnification, 3 μs pixel-dwell time (frame time accounting for flyback was 3.78 s) and beam currents of 6.2 pA (left and right) and 3.9 pA (middle), corresponding to 34.2 e^-/nm^2f (left and right) and 21.6 e^-/nm^2f (middle).

Initially, the growth rate and number of particles formed were both high (Fig. 6 left). As the dose per frame was lowered, the number of particles nucleated consistently diminished (Fig. 6 middle). After a number of consecutive experiments on the same chip, the growth of particles slowed with time due to consumption of silver precursor. When the initial electron dose rate conditions were used, similar growth rates and numbers of nanoparticles were not reproduced (Fig. 6 right). Instead, slower growth and fewer particles with more spherical shapes were observed. Solution depletion and the increasing number of excess unreacted radicals in solution likely altered the growth rates measured and modified the experiments over time. One method to mitigate this problem could be to replenish the solution with new precursor using the flow capabilities of the liquid holder. However, depending on the wettability of the solution, the spacing between chips, local surface chemistry of the membranes, or the presence of solid matter, there is no guarantee that the solution will fully fill the chamber. Other methods that could alleviate depletion would be to maximize the space between experimental areas on the liquid cell chip, increase the volume of liquid, or make use of only the first scans of each session for quantitative analysis. Fig. 6 demonstrates that sample history has a large effect on *in situ* experiments and if uncontrolled, may hinder quantification and limit reproducibility by producing a hysteresis in the growth rates. For example, the effect of solution depletion is evident during in situ growth of dendritic gold at the nanoscale,[22] where most tips velocities were measured to be an order of magnitude slower than what expected in models for diffusion-limited growth.

4. Reactivity of the Solution

While image analysis algorithms can be applied to any *in situ* dataset to quantify the change over time of a specific feature in the images, it is the interpretation of such analysis that provides physical meaning to the observations. As explained above, the electron beam may modify the experiment and change the chemistry of the solution. Therefore, it is important in all liquid experiments to verify that the reaction observed *in situ* corresponds to the reaction being quantified. The presence of impurities or contamination, and differences arising from the radical chemical processes induced by the electron beam-liquid

interaction may modify the experiment and produce undesired growth of particles apart from the anticipated reaction.[18] In some cases, growth of particles may occur when the solution is expected to be completely unreactive. Fig 7 (a) shows a dark field (DF) STEM image of ZSM-5 zeolite (aluminoslicate) particles in water. Clearly defined zeolite particles on the order of ~50 nm are attached to the top window, while out of focus particles are attached to the bottom window. Streaking in the image suggests that some zeolites are mobile in the water. These particles were all present when the beam was turned on and the solution was imaged.
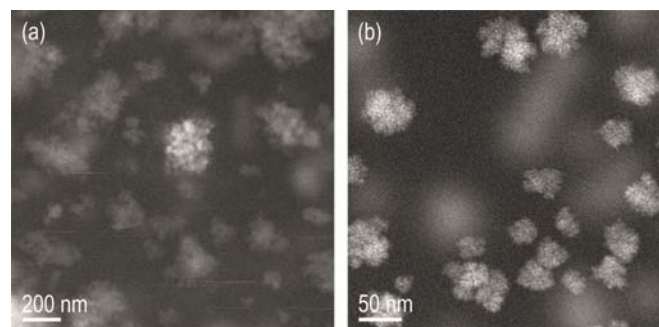

Fig. 7. DF STEM images of mesoporous zeolite nanoparticles in water (a), and silica nanoparticles grown *in situ* from the same solution as for (a) after being store for about one year (b). A beam current of 5.6 pA was used for both experiments. Images were acquired using an electron dose per frame of 334 e^-/nm^2f (a) and 2866 e^-/nm^2f (b). Despite the similarities in morphology and size, no traces of aluminium were found in particles grown *in situ* using the electron beam.

The same water/zeolite solution used for Fig. 7 (a) was stored for approximately one year and imaged once more in the (S)TEM. In this second experiment, the solution was not reactive and after continued STEM illumination, particles growed under the electron beam. The final product of one of these *in situ* growth experiments is shown in Fig. 7 (b). The particles grown, similar to those in the image from the fresh solution in Fig. 7 (a), were located on both SiN windows, with similar morphology and size range (20 − 100 nm). However, when the chips were washed and inserted into the SEM for EDX ex-situ analysis, no aluminium was found. The particles grown during *in situ* experiments appear to be silica and not zeolites. Thus, without performing "post mortem" analysis on the products of *in situ* growth, any results obtained during the growth process are prone to misinterpretation.

5. Conclusions

Studying dynamic processes such as self-assembly, nucleation and growth of nanoparticles, conformational dynamics in biological systems, or the fundamental mechanisms of lithium-ion batteries in operation in non-aqueous electrolytes, require characterization tools able to provide *in situ* information with nanometer spatial resolution in liquids. This can be achieved using fluid stages in the (S)TEM. Methods of measuring the amount of radiation damage resulting from beam-induced reactions with the sample are needed to correctly interpret quantitative information. Besides that, reproducing a result in a different instrument operating with different electron optical settings introduces a whole range of parameters that must be taken into account. Increasing the electron dose increases the

number of radicals in solution and can trigger adverse chemical reactions. On the other hand, when increasing the energy of the incident electrons (acceleration voltage), two opposing factors are identified. While the morphology of the resulting nanocrystals suggests that the amount of radicals produced may be higher for the case of lower beam energies, the decrease in number of nucleation sites does not support this observation, suggesting that a more thoughtful analysis of this effect is required, possibly one including oxidation back reactions. While controlling dose in STEM is already a straightforward procedure, the typical electron doses used in TEM mode correspond to a much higher number of electrons delivered to the sample than their equivalent values in STEM. However, in terms of cumulative dose, similar results should be achievable with low dose techniques. Formation of bubbles and subsequent increase of resolution is indicative of high doses. The effect of cumulative dose after subsequent experiments and precursor solution depletion must be considered and avoided for every *in situ* result, and corresponding post-mortem analysis of reaction products will help to avoid misleading interpretations.

6. Experimental

In situ STEM and TEM images and movies were acquired using an 80-300 kV FEI probe Cs-corrected Titan transmission electron microscope equipped with an electron gun monochromator and a Gatan Quantum ERS spectrometer. A Hummingbird Scientific fluid stage was used for all the liquid experiments performed. For the silver growth experiments, two silicon chips with 50 nm thick membranes and one of them with 500nm spacers (Hummingbird Scientific) were used. For observation of zeolite nanoparticles and *in situ* growth of silica, two blank chips were used, with the liquid spacing created by particles on the silicon chip surface. The electron beam current measured in the screen dose-meter of the microscope was calibrated to obtain the exact electron current values at the sample plane using an analytical holder with incorporated faraday cup (Gatan, Inc.) Silver nitrate ($AgNO_3$) precursor solutions with a concentration of 0.1 mM were prepared using Millipore grade DI water as described previously.[4]

The beam and microscope parameters used for calculation of the electron dose per frame in STEM imaging mode are the electron beam current, pixel dwell time and magnification (pixel size). The dose per frame is given in units of (electrons/nm^2) and in this manuscript will be described as (electrons/(nm^2·f)), where f indicates that the dose is calculated for each frame in the *in situ* movie. For STEM imaging mode, the dose per frame is calculated by dividing the calibrated beam current at the sample, i_e (C/s), by the size of the viewing area and multiplying by the frame time as follows: $(i_e \cdot t_f)/(e \cdot A)$, where A is the scan area (nm^2), e is the elementary charge (C/electron) and t_f is the frame time. While other definitions of dose would consider the probe size instead of the scan area, here we use the latter as a standard value to 1) avoid the complexity of beam broadening issues dependent on the specifics of the experiment and 2) to minimize the problem of undersampling or oversampling when changing magnification. (Further details on the calculation of the electron dose rate in STEM can be found in[4]). For instance, in order to calculate the dose per frame for the STEM dataset in Fig 3(a), we would first calculate the frame size by multiplying the image size (1024x1024 pixels) by the pixel size (4.1nm^2): $A = 4.3 \cdot 10^6$ nm^2. Taking into account that the calibrated beam current was $i_e =$

3.5 pA and the frame time was $t_f = 3.78$ s (see Table I) and e = $1.602 \cdot 10^{-19}$ C/electron, then the dose per frame yields: $[(3.5 \cdot 10^{-9}) \cdot 3.78]/(1.602 \cdot 10^{-19} \cdot 4.3 \cdot 10^6) = 19.5$ e^-/nm^2f.. In TEM, the dose rate per frame and pixel was estimated by dividing the calibrated beam current in TEM, i_e (C/s), by the size of the illuminated area on the sample, A·(nm^2), and multiplying by the exposure time, t_{exp} (s): $(i_e \cdot t_f)/(e \cdot A)$.

Further details on image acquisition, sample loading and choice of microscope parameters can be found in previous publications[3, 4, 6, 18].

Notes and references

[a] Fundamental and Computational Sciences Directorate, Pacific Northwest National Laboratory, P.O. Box 999, Richland, WA 99352, USA.

[b] Department of Chemical Engineering and Materials Science, University of California-Davis, One Shields Ave., Davis, CA 95616, USA.

[c] Environ. Molecular Sci. Lab., Pacific Northwest National Laboratory, Richland, WA 99352, USA.

[d] Energy and Environmental Directorate, Pacific Northwest National Laboratory, P.O. Box 999, Richland, WA 99352, USA.

*Current author address: Division of Materials Science and Engineering, Ames DOE Laboratory, Ames, IA 50011, USA.

1. M. J. Williamson, R. M. Tromp, P. M. Vereecken, R. Hull and F. M. Ross, *Nat Mater*, 2003, 2, 532-536.
2. E. R. White, S. B. Singer, V. Augustyn, W. A. Hubbard, M. Mecklenburg, B. Dunn and B. C. Regan, *Acs Nano*, 2012, 6, 6308-6317.
3. J. E. Evans, K. L. Jungjohann, N. D. Browning and I. Arslan, *Nano Letters*, 2011, 11, 2809-2813.
4. T. J. Woehl, J. E. Evans, L. Arslan, W. D. Ristenpart and N. D. Browning, *Acs Nano*, 2012, 6, 8599-8610.
5. H. G. Liao, L. K. Cui, S. Whitelam and H. M. Zheng, *Science*, 2012, 336, 1011-1014.
6. L. R. Parent, D. B. Robinson, T. J. Woehl, W. D. Ristenpart, J. E. Evans, N. D. Browning and I. Arslan, *Acs Nano*, 2012, 6, 3589-3596.
7. K. L. Jungjohann, S. Bliznakov, P. W. Sutter, E. A. Stach and E. A. Sutter, *Nano Letters*, 2013, 13, 2964-2970.
8. L. R. Parent, D. B. Robinson, P. J. Cappillino, R. J. Hartnett, P. Abellán, J. E. Evans, N. D. Browning and I. Arslan, *Chemistry of Materials*, 2014, DOI: 10.1021/cm4035209.
9. J. E. Evans, K. L. Jungjohann, P. C. K. Wong, P.-L. Chiu, G. H. Dutrow, I. Arslan and N. D. Browning, *Micron*, 2012, 43, 1085-1090.
10. U. M. Mirsaidov, H. M. Zheng, Y. Casana and P. T. Matsudaira, *Biophys J*, 2012, 102, 386a-387a.
11. Q. Chen, J. Smith, J. Park, S. Lee, K. Kim, A. Zettl and A. P. Alivisatos, *Abstr Pap Am Chem S*, 2013, 245.

12. T. W. Huang, S. Y. Liu, Y. J. Chuang, H. Y. Hsieh, C. Y. Tsai, W. J. Wu, C. T. Tsai, U. Mirsaidov, P. Matsudaira, C. S. Chang, F. G. Tseng and F. R. Chen, *Soft Matter*, 2013, 9, 8856-8861.
13. M. T. Proetto, A. M. Rush, M.-P. Chien, P. Abellan Baeza, J. P. Patterson, M. P. Thompson, N. H. Olson, C. E. Moore, A. L. Rheingold, C. Andolina, J. Millstone, S. B. Howell, N. D. Browning, J. E. Evans and N. C. Gianneschi, *J Am Chem Soc*, 2014, DOI: 10.1021/ja408513m.
14. K.-L. Liu, C.-C. Wu, Y.-J. Huang, H.-L. Peng, H.-Y. Chang, P. Chang, L. Hsu and T.-R. Yew, *Lab on a Chip*, 2008, 8, 1915-1921.
15. N. de Jonge, D. B. Peckys, G. J. Kremers and D. W. Piston, *Proceedings of the National Academy of Sciences*, 2009.
16. M. Gu, L. R. Parent, B. L. Mehdi, R. R. Unocic, M. T. McDowell, R. L. Sacci, W. Xu, J. G. Connell, P. Xu, P. Abellan, X. Chen, Y. Zhang, D. E. Perea, J. E. Evans, L. J. Lauhon, J.-G. Zhang, J. Liu, N. D. Browning, Y. Cui, I. Arslan and C.-M. Wang, *Nano Letters*, 2013, 13, 6106-6112.
17. N. de Jonge and F. M. Ross, *Nat Nanotechnol*, 2011, 6, 695-704.
18. T. J. Woehl, K. L. Jungjohann, J. E. Evans, I. Arslan, W. D. Ristenpart and N. D. Browning, *Ultramicroscopy*, 2013, 127, 53-63.
19. Y. Liu, K. Tai and S. J. Dillon, *Chemistry of Materials*, 2013, 25, 2927-2933.
20. H. M. Zheng, S. A. Claridge, A. M. Minor, A. P. Alivisatos and U. Dahmen, *Nano Letters*, 2009, 9, 2460-2465.
21. E. A. Ring and N. de Jonge, *Micron*, 2012, 43, 1078-1084.
22. T. Kraus and N. de Jonge, *Langmuir*, 2013, 29, 8427-8432.
23. E. R. White, M. Mecklenburg, B. Shevitski, S. B. Singer and B. C. Regan, *Langmuir*, 2012, 28, 3695-3698.
24. U. M. Mirsaidov, H. M. Zheng, Y. Casana and P. Matsudaira, *Biophys J*, 2012, 102, L15-L17.
25. K. L. Jungjohann, J. E. Evans, J. A. Aguiar, I. Arslan and N. D. Browning, *Microsc Microanal*, 2012, 18, 621-627.
26. J. Belloni, *Catal Today*, 2006, 113, 141-156.
27. E. R. White, M. Mecklenburg, S. B. Singer, S. Aloni and B. C. Regan, *Appl Phys Express*, 2011, 4.
28. M. Adrian, J. Dubochet, J. Lepault and A. W. Mcdowall, *Nature*, 1984, 308, 32-36.
29. B. Pastina and J. A. LaVerne, *J Phys Chem A*, 2001, 105, 9316-9322.
30. D. Williams and C. B. Carter, in *Transmission Electron Microscopy*, Springer US, 2009, DOI: 10.1007/978-0-387-76501-3_1.
31. D. B. Carlson and J. E. Evans, in *The Transmission Electron Microscope*, ed. K. Maaz, InTech, http://www.intechopen.com/books/the-transmission-electron-microscope/low-dose-imaging-techniques-for-transmission-electron-microscopy, 2012, DOI: 10.5772/36614.
32. N. de Jonge, N. Poirier-Demers, H. Demers, D. B. Peckys and D. Drouin, *Ultramicroscopy*, 2010, 110, 1114-1119.
33. K. L. Klein, I. M. Anderson and N. De Jonge, *Journal of Microscopy*, 2011, 242, 117-123.